Optimal Local-Loop Shaping and Signal Reconstruction Beyond Nyquist Frequency under Non-Integer Sampling Ratios ⋆

Thomas L. Chu† Xiaohai Hu† Xu Chen†,⋆

Mechanical Engineering Department, University of Washington, Seattle, WA 98195

Abstract

At the core of feedback control is shaping the closed loop's error rejection function. This is particularly crucial in high-precision motion control, where attenuation notches are often introduced in the sensitivity function to suppress band-limited disturbances. However, classical control struggles as the disturbance approaches or exceeds the Nyquist frequency of the feedback sensor. In particular, it remains not well understood how to address situations when non-integer sampling ratios exist among the sub control system modules. In this paper, we propose a new framework and solution steps for non-integer sampling-based signal processing and synchronization, along with an optimal control design to reject structured disturbances beyond the Nyquist frequency. This is achieved with a novel coprime factorization that removes the restriction in fast-to-slow sampling-period conversion, a Youla-Kučera parameterization and convexification for loop shaping with prescribed stability and optimality, and a tailored design with finite and infinite impulse response filters. Experimental validation on motor control hardware demonstrates the effectiveness for structured signal reconstruction beyond-Nyquist frequency, achieving over 60% reduction in root mean square error under measurement noise. In addition, simulations on an in-house galvanometer scanning system verify that the proposed method improves disturbance attenuation performance and robustness to noise, achieving over 90% band-limited disturbance attenuation beyond the Nyquist frequency.

Key words: Vibration and modal analysis, Nyquist frequency, signal processing, filtering.

1 Introduction

An essential task in precision motion control is to shape the feedback loop locally to reject band-limited disturbances. Such local-loop shaping (LLS) is crucial in high-precision applications such as servo control in hard disk drives (HDDs) and semiconductor photolithography, where nanometer-scale positioning accuracy is required [37, 13]. At its core, LLS introduces attenuation notches at the disturbance frequency in the closed-loop error rejection function while adhering to the inherent limitations of feedback control design. Such design of the error-rejection function can be achieved, for example, with the use of disturbance observers (DOBs), which provides an intuitive structure via explicit [27, 4] and implicit [19] model inversion, leading to deep applications in precision manufacturing and information storage systems [7, 17, 39, 46].

⋆ † T. L. Chu (email: tchu@uw.edu), X. Hu (email: huxh@uw.edu) and X. Chen (email: chx@uw.edu) are with the Mechanical Engineering Department, University of Washington, Seattle, WA 98195. ⋆: corresponding author.

Traditional LLS becomes fundamentally limited when the feedback sensing rate lags behind the system dynamics. In such cases, disturbances beyond the sensor's Nyquist frequency are not fully observable due to aliasing. This limitation is increasingly significant, e.g., in vision-based sensing systems, where the sensor data and speed impose substantial computational burdens and communication constrains [36]. These limitations appear in a wide range of applications, including robotic visual servoing with sensing latency constraints [11], selective laser sintering (SLS) with slow thermal sensing [42], vibration rejection during position tracking in aerospace systems [25, 38, 31], and sub-Nyquist sampling problems in ultrasound images [20, 10], radio communication [45, 47], and power grid management [21, 32].

Recent advances in control strategy have explored compensation of disturbances beyond the Nyquist frequency. Systems using multiple slow-rate sensors at different sampling rates can exceed the Nyquist frequency of a single-rate slow-sampled sensor [2, 16]. In the case of multirate systems with only a single fast-sampled input and slow-sampled output, recursive least squares

[28] and weighted sinusoidal inputs [44, 43] have been proposed to address beyond-Nyquist modeling and disturbance attenuation.

Despite the increasing recognition of beyond-Nyquist controls, existing explorations are primarily made under an integer-ratio assumption, where the fast- and slow-sampling periods maintain a fixed periodic alignment (e.g., the sensor speed is 3 or x times slower than the control speed). However, for increasing systems involving vision or other types of slow feedback under wired or wireless communications [34, 41], maintaining fixed integer-ratio sampling and synchronization between subsystems is intrinsically challenging and can be even impractical. Approximating these fractional-rate systems using integer ratios, on the other hand, is nontrivial and introduces timing mismatch. Such timing errors can produce a spectral distortion that becomes increasingly significant at high frequencies and near the Nyquist frequency [33]. Therefore, beyond-Nyquist signal processing and controls under fractional sampling remain a complex challenge with asynchronous timing, aliasing, and robustness constraints.

With the pressing needs from practical systems on the one hand, and the theoretical challenges of modeling and control on the other, this paper provides a novel beyond-Nyquist signal processing and loop shaping for optimal structured disturbance rejection under non-integer sampling relationships. The core consists of (i) a model-based signal processing and synchronization via a multirate model predictor (MMP) that leverages the Internal Model Principle, and (ii) a Youla-Kučera parameterization using the structure of a forward model multirate disturbance observer (MFMDOB), to collectively achieve beyond-Nyquist disturbance rejection while preserving closed-loop stability. To cope with the aliasing-induced amplification and reconstruction error, we then introduce an optimal filter parameterization to ensure disturbance rejection at the target frequencies, while simultaneously reducing sensitivity amplification across the frequency spectrum. What may be initially surprising, is that the resulting signal processing achieves an equivalent sampling rate that is multiple times beyond even the fastest rate in the original feedback system. This comes from a unique yet nontrivial coprime factorization in the proposed non-integer sampling, leading to a highly capable wide-frequency compensation range.

The main contributions of this work are:

- A first-of-its-kind high-frequency discrete-time signal recovery method beyond the limit of conventional integer-rate sampling;
- A novel coprime factorization framework to address beyond-Nyquist signal processing in a feedback system;
- A new forward model multirate disturbance observer (MFMDOB) for non-minimum phase (NMP) systems with an optimally filter design workflow for beyond-Nyquist disturbance rejection;
- Comprehensive validation through hardware and simulation testing, with improvement in reconstruction accuracy and reduced sensitivity to noise by over 60% and over 90% reductions, respectively, in root mean square (RMS) error.

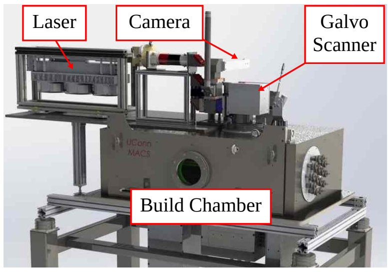

(a)

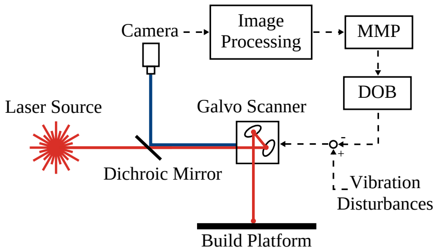

(b)

Fig. 1. Model of the in-house built laser powder bed fusion (subfigure a) and illustration of the SLS process with visual feedback and the proposed disturbance observer (subfigure b). The camera is used to track the beam position but with a slow-sampling rate—susceptible to substantial beyond-Nyquist vibrations.

The remainder of this paper is structured as follows. Section 2 introduces notation and the MFMDOB design. We propose the algorithm for the MMP and introduce the optimal filter parameterization in Sections 3 and 4, respectively. Experimental validation is presented in Section 5. Finally, we conclude the paper in Section 6.

2 Problem Formulation

We demonstrate the proposed MMP on a motor control hardware and MFMDOB in simulation on the laser beam steering control of an in-house developed selective laser sintering (SLS) additive manufacturing testbed (Figure 1).

Figure 2 shows the block diagram of the overall addressed problem and the proposed controller structure. We index continuous-time signals by (t), discrete-time signals by $[n]$ (e.g. $y(t)$ and $y[n]$ are the continuous- and discrete-time outputs, respectively, with $n \in \mathbb{Z}^+$). Ignoring the inner loop from $\hat{P}(z)$ to $Q(z)$, we have a standard

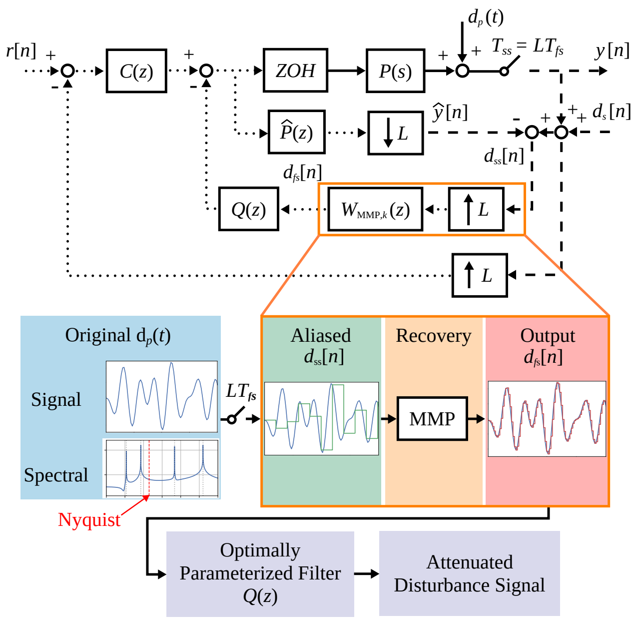

Fig. 2. Block diagram of the proposed MFMDOB. The sampling periods are indicated by the dashed (slower, $T_{ss} = LT_{fs}$) and the dotted (faster, T_{fs}) lines. The MMP signal reconstruction process is denoted by $W_{\mathrm{MMP},k}(z)$ where the input is the slow-sampled signal, and the output is the reconstructed signal.

feedback system with a reference input $r[n]$, a baseline controller $C(z)$, a zero-order hold (ZOH), and the controlled plant $P(s)$. *Our focus is on the challenging situation where 1) the plant output $y[n]$ is sampled at a slow period T_{ss}, 2) the disturbance $d_p(t)$ contains major components beyond the Nyquist frequency $1/(2T_{ss})$, and 3) the controller may operate at a clock rate T_{fs} that is faster than T_{ss}.* In addition, we focus on disturbance signals with an underlying structure that is partially known to us. This will be made more specific in the next section. [1]

Adding the inner-loop components and an illustration of the mixed-rate signal flows, we have the proposed MFMDOB in Fig. 2. The MFMDOB uses principles from internal model control, where the forward model is leveraged and the inverse dynamics of the plant is parameterized through a performance-enhancement Q filter. [2] More specifically, we introduce: $\hat{P}(z)$—the discrete-time T_{fs} fast-sampled ZOH equivalence of $P(s)$; $W_{\mathrm{MMP},k}(z)$—an MMP that can losslessly reconstructed the focused class of disturbances beyond the Nyquist frequency, shaping a T_{ss} slow-sampled input $d_{ss}[n]$ to an estimated fast disturbance $d_{fs}[n]$ sampled at T_{fs}; $Q(z)$—an optimally designed Q filter that counteracts the effect of disturbance beyond the Nyquist frequency of the original output sampler; and $d_p(t)$ and $d_s[n]$—the plant disturbances and the sensor noise, respectively.

Mathematically, we map the slow- and fast-sampling period as $T_{ss} = LT_{fs}$, where L is a non-integer rational number. This is a rather general assumption that applies to broad application scenarios.

In addition to the aforementioned notation and signal flows, we use $\boxed{\uparrow L}$ and $\boxed{\downarrow L}$ as to indicate upsampling and downsampling operations, respectively. One can observe that the $\hat{P}(z)$ and $\boxed{\downarrow L}$ blocks generate $\hat{y}[n]$, an estimated disturbance-free output sampled at the slow T_{ss}. [3] Then, at the summing junction after $\hat{y}[n]$, the output $d_{ss}[n] = y[n] - \hat{y}[n] + d_s[n]$, where the effect of the control input gets canceled out, yielding an estimate of the disturbance $d_p(nLT_{fs}) + d_s[n]$. After processing the disturbance-information-rich $d_{ss}[n]$ with the proposed mixed-rate optimal fractional-order signal processing, $Q(z)$ outputs a fast compensation command that is fed back to the input-side of the plant.

Besides the inner-loop configuration in Fig. 2, the proposed algorithm can also be implemented as an outer-loop controller as shown in Fig. 3. Analogous analysis will apply. Such a form is useful when it is inconvenient or infeasible to change the internal baseline controls.

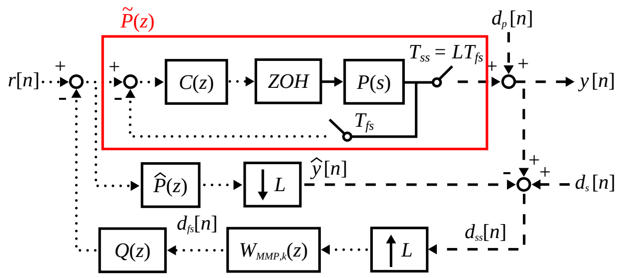

Fig. 3. Alternative form of the proposed controller structure, with the controller embedded within the plant.

3 Signal Reconstruction for Non-Integer Sampling Ratios

3.1 *The Proposed Fractional-Sampling Temporal Mapping*

3.1.1 *A coprime sampling factorization and synchronization*

Recall the definition of the rational sampling ratio L in the previous section. Let $L = N_L/D_L$, where $N_L > D_L$,

[1] If a completely stochastic broadband disturbance appears beyond the Nyquist frequency, little control could be done; and from a loop shaping viewpoint, it is best to apply less control (small gain) at high frequencies.

[2] When all signals have the same sampling rate, the inner-loop structure is in fact a form of Youla-Kučera all-stabilizing control [15].

[3] The $\hat{P}(z)$ and $\boxed{\downarrow L}$ blocks are introduced for analysis purposes. In practice, these two blocks can be implemented as one slow-sampled ZOH equivalent of $P(s)$ at T_{ss}.

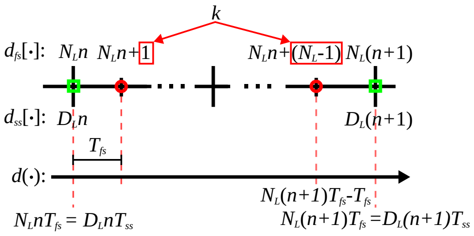

Fig. 4. Relationship between fast- and slow-sampling periods for non-integer factors. The slow-sampled signal (green squares) and fast-sampled signal (red circles) synchronizes at $d_{ss}[D_L n] = d_{fs}[N_L n] = d(N_L n T_{fs})$. k denotes the inter-sample point between $d_{ss}[D_L n]$ and $d_{ss}[D_L(n+1)]$ and spans from $1, \ldots, N_L - 1$.

and N_L and D_L are coprime integers. Such N_L and D_L always exist as long as L is rational, i.e. $L \in \mathbb{R}$. By this treatment of the sampling ratio, and recalling the relationship between the slow and fast sampling periods $T_{ss} = LT_{fs}$, we have

$$D_L T_{ss} = N_L T_{fs}. \tag{1}$$

We then have the key relationship between the fast- and slow-sampled signals:

$$d_{fs}[N_L n] = d_{ss}[D_L n] \,, \tag{2}$$
$$d_{ss}[n] = d_p(nLT_{fs}) \,, \tag{3}$$

where Eq. (3) establishes the mapping between the continuous-time plant disturbance $d_p(t)$ to the slow-sampled discrete-time $d_{ss}[n]$; and Eq. (2) comes from the relationship $d_{fs}[N_L n] = d_p(N_L n T_{fs}) = d_p(D_L n T_{ss}) = d_{ss}[D_L n]$ after applying Eq. (1). Furthermore, applying Eq. (1) again, we have $d_{fs}[N_L(n+1)] = d_p(N_L n T_{fs} + N_L T_{fs}) = d_p(D_L n T_{ss} + D_L T_{ss}) = d_{ss}[D_L(n+1)]$. With these results, we obtain a consistent mapping between the slow- and fast-sampled signals, as illustrated in Fig. 4. In particular, synchronization between the slow- and fast-sampled signals occurs sparsely, and exact alignment occurs once every N_L fast-sampling intervals (or equivalently every D_L slow-sampling intervals).

We define $k \in \{1, \ldots, N_L - 1\}$, which denotes the k^{th} inter-sample point between consecutive synchronization instants $d_{fs}[N_L n]$ and $d_{fs}[N_L(n+1)]$. Based on what we derived in the last paragraph, $N_L - 1$ inter-sample points must be reconstructed between consecutive aligned slow-sampled measurements $d_{ss}[D_L n]$ and $d_{ss}[D_L(n+1)]$.

3.1.2 General signal modeling

We construct the MMP based on the internal-model concept, where a discrete-time structured signal can be represented as the output of a linear system driven by an impulse signal $\delta[n]$ [26]. For example, a constant $d[n] = d$ corresponds to the impulse response of the scaled integrator $d/(1 - z^{-1})$, while $\sin(\omega n)$ corresponds to the impulse response of the filter $(z^{-1}\sin\omega)/(1 - 2z^{-1}\cos\omega + z^{-2})$. More generally, we model the disturbance as [9, 42]

$$d[n] = \frac{B_d(z^{-1})}{A_d(z^{-1})}\delta[n] \,, \tag{4}$$

where z^{-1} denotes the backward shift operator [12]. Rewriting Eq. (4) as $A_d(z^{-1})d[n] = B_d(z^{-1})\delta[n]$, we have the right-hand side as a finite linear combination of delayed, weighted impulses that vanishes for $n > 0$, implying

$$A_d(z^{-1})d[n] \to 0 \,. \tag{5}$$

Equation (5) reflects the internal structure of the disturbance and forms the basis for perfect multirate disturbance rejection. In particular, we will show that it enables the construction of an analytically solvable Diophantine equation that recovers the structured disturbance at fractional intervals of the slowing period.

3.1.3 Disturbance modeling under fractional sampling

We now formulate the disturbance-model polynomial $A_d(z^{-1})$ for fractional sampling. Moving forward, we will only require knowledge of $A_d(z^{-1})$, i.e., the denominator in Eq. (4).

Consider a plant disturbance consisting mainly of m narrow-band components in the form of

$$d_p(t) = d_b(t) + \sum_{i=1}^{m} \lambda_{d,i} \sin\left(2\pi f_{d,i} t + \phi_{d,i}\right) \,, \tag{6}$$

where $\lambda_{d,i}$ and $\phi_{d,i}$ are unknown amplitudes and phase shifts of the narrow-band disturbance components, and $d_b(t)$ represents broad-band noises. The disturbance frequency, $f_{d,i}$ (Hz), can be acquired via spectrum analysis or system identification and is assumed to be known or can be adaptively estimated [5, 22]. After sampling at a fast rate of T_{fs} sec, the narrow-band part of the disturbance-model polynomial $A_d(z^{-1})$ is given by

$$\begin{aligned} A_d(z^{-1}) &= \prod_{i=1}^{m} \left(1 - 2\cos(2\pi f_{d,i} T_{fs}) z^{-1} + z^{-2}\right) \,, \\ &\triangleq 1 + a_1 z^{-1} + \ldots + a_{2m} z^{-2m} \,. \end{aligned} \tag{7}$$

After we establish the analysis pipeline, such a model structure will apply quickly to wide-band disturbances such as those in [4, 19, 18, 30, 8, 6].

3.2 Fractional-Sampling Multirate Model Predictor

Under Eq. (4), the proposed MMP reconstructs band-limited signals at prescribed fractional rates of the slow-sampling period for a non-integer L using past slow-sampled signals and historical inter-sample estimates.

Theorem 1 *Let $d_{fs}[N_L n + k]$, $k \in (1, \ldots, N_L - 1)$, denote the k^{th} inter-sample between $d_{fs}[N_L n]$ and $d_{fs}[N_L(n+1)]$. Let m denote the number of distinct frequencies in $d_p(t)$. Then,*

$$\begin{aligned} d_{fs}[N_L n + k] =& \sum_{i=0}^{n_w} w_{k,i} d_{ss}[(n-i)D_L] \\ & - \sum_{j=1}^{2m} b_j d_{fs}[(n-j)N_L + k] \;, \end{aligned} \tag{8}$$

where the coefficients b_j are defined by

$$\begin{aligned} B^*(z^{-N_L}) =& -1 + \prod_{i=1}^{m} \big(1 - 2\alpha \cos(2\pi N_L T_{fs} f_{d,i}) z^{-N_L} \\ & + \alpha^2 z^{-2N_L}\big) \;, \\ \triangleq & b_1 z^{-N_L} + \ldots + b_{2m} z^{-2mN_L} \;, \end{aligned} \tag{9}$$

and the coefficients $w_{k,i}$'s form a filter $W_k(z^{-N_L})$ that is solved from the following special Diophantine equation:

$$F(z^{-1})A_d(z^{-1}) + z^{-k} W_k(z^{-N_L}) - B^*(z^{-N_L}) = 1 \,.$$

Derivation of Eq. (8)*, solution of the Diophantine equation, and Proof of the Theorem are provided in Appendix A.*

Signal reconstruction is feasible provided that at least $2m$ past slow-sampled signals (i.e. $n_w \geq 2m - 1$) and $2m$ historical inter-sample estimates are available.

Remark 2 *The proposed fractional-order MMP is an infinite-impulse-response (IIR) structure, as the reconstructed signal depends on the feedback from historical inter-sample estimates. This behavior is reflected in the following transfer function form of Eq.* (8)*:*

$$W_{MMP,k}(z) = \frac{w_{k,0} + w_{k,1} z^{-N_L} + \ldots + w_{k,n_w} z^{-n_w N_L}}{1 + b_1 z^{-N_L} + \ldots + b_{2m} z^{-2mN_L}} . \tag{10}$$

To be more specific, noting the fast- and slow-sampling periods of d_{fs} and d_{ss}, we can write Eq. (8) *equivalently as $d_{fs}(N_L T_{fs} n + kT_{fs}) = \sum_{i=0}^{n_w} w_{k,i} d_{ss}((n-i)D_L T_{ss}) - \sum_{j=1}^{2m} b_j d_{fs}((n-j)N_L T_{fs} + kT_{fs})$. Applying Eq.* (1) *yields $d_{fs}(N_L T_{fs} n + kT_{fs}) = \sum_{i=0}^{n_w} w_{k,i} d_{ss}((n-i)N_L T_{fs}) - \sum_{j=1}^{2m} b_j d_{fs}((n-j)N_L T_{fs} + kT_{fs})$. Hence, in the T_{fs}-sampled discrete-time domain, $d_{fs}[N_L n + k] = \sum_{i=0}^{n_w} w_{k,i} d_{ss}[(n-i)N_L] - \sum_{j=1}^{2m} b_j d_{fs}[(n-j)N_L + k]$, whose transfer function from d_{ss} to d_{fs} is Eq.* (10)*.*

From the same theorem, we can have a finite-impulse-response (FIR) solution by omitting the historical inter-sample estimates (i.e., setting $\alpha = 0 \Rightarrow B^*(z^{-N_L}) = 0$ in Eq. (9)*), thereby constraining the inter-sample estimates to depend solely on past slow-sampled measurements.*

Remark 3 *The choice of the tunable parameter, $\alpha \in (0,1)$, determines the pole locations of $B^*(z^{-N_L})$, allowing independent adjustment for sensitivity to noise, namely, α is used to adjust the bandwidth of the MMP. As $\alpha \to 1$, the bandwidth narrows. Increasing α to 1 also causes the poles of $W_{\mathrm{MMP},k}(z)$ to approach the unit circle. Consequently, the transient response time for the signal reconstruction increases.*

3.3 Multi-Phase Signal Reconstruction

Equation (8) reconstructs the fast-sampled structured d_p signal using only every D_L^{th} slow-sampled measurement when L is non-integer, resulting in a sparse measurement structure. To incorporate all available slow-sampled measurements, we extend the reconstruction to be a D_L- phase structure, where each recovery algorithm is one residue class of the slow-sampled signal. This requires D_L reconstruction phases, each initialized one slow-sampling period T_{ss} apart and operating on the signal subsequences $d_{ss}[D_L n + j]$ $\forall j = 0, \ldots, D_L - 1$. Each phase produces $N_L - 1$ inter-sample estimates between consecutive slow-sampled signals, and the combined phases form an *effective sampling periods* of $T_{es} = T_{fs}/D_L$—substantially beyond even the fast sampling period of the original feedback loop. Algorithm 1 details the steps of the multi-phase signal reconstruction.

Algorithm 1 Multi-phase signal reconstruction for non-integer L

1: **Input:** Slow-sampled signal $d_{ss}[n]$, parameters D_L, N_L, coefficients $w_{k,i}$ and b_i
2: **Output:** Reconstructed fast-sampled signal $d_{fs}[n]$
3: **for** $j = 0, 1, \ldots, D_L - 1$ **do**
4:   Initialize phase j using subsequence $d_{ss}[D_L n + j]$
5: **end for**
6: **for** each slow-sample index n **do**
7:   **for** $j = 0, 1, \ldots, D_L - 1$ **do**
8:     Compute inter-sample estimate using Eq. (8)
9:   **end for**
10: **end for**
11: Sum phase outputs to obtain reconstructed signal $d_{fs}[n]$
12: Resulting effective sampling period: $T_{es} = T_{fs}/D_L$

Consider an example in Fig. 5, where $L = 2.5$, yielding $N_L = 5$ and $D_L = 2$. The first reconstruction is initiated at $d_{ss}[0]$ and operates on the even-indexed subsequences $d_{ss}[2n]$, $n \in \mathbb{Z}^+$. After one slow-sampling period, the second reconstruction algorithm is initiated at $d_{ss}[1]$ and operates on the odd-indexed subsequences $d_{ss}[2n+1]$, $n \in \mathbb{Z}^+$. Each phase reconstructs the inter-samples corresponding to its alignment pattern, and the two reconstructed signals are temporally offset by T_{ss}.

By combining these complementary signals, all slow-sampled measurements are used to form the recovered signal with effective sampling period of $T_{es} = T_{fs}/2$, creating an ability to operate beyond the fastest sampling frequency in the original feedback loop.

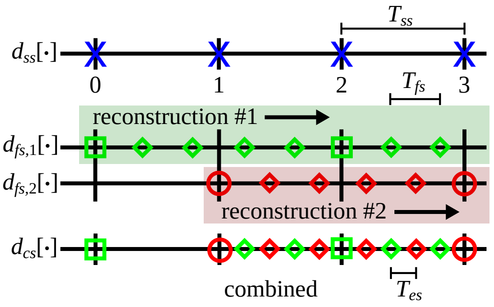

Fig. 5. Multi-phase reconstruction where $L = 2.5$.

3.4 *Verification*

3.4.1 *Experimental Validation*

We perform online experimental validation of the multi-phase signal reconstruction using a MinSegMotor equipped with an Arduino Mega 2560 and an encoder sampling at 8 Hz,[4] shown in Fig. 6. A 7 Hz sinusoidal reference with amplitude 2 V (normalized to unity magnitude) was applied to the motor, resulting in an aliased position measurement since the Nyquist frequency of the encoder is only 4 Hz. Encoder measurements were acquired through hardware-in-loop monitoring with the Simulink Support Package for Arduino. The experimental parameters are summarized in Table 1.

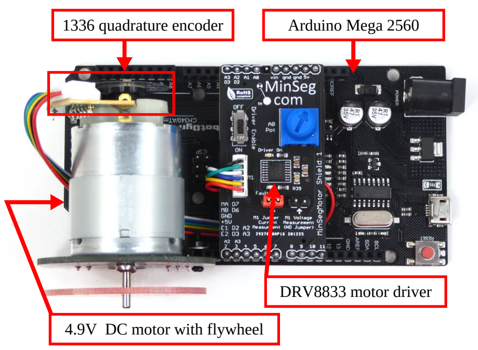

Fig. 6. Experimental platform with a MinSegMotor using an Arduino Mega 2560 board with a 1336 quadrature encoder count.

[4] For illustrating the beyond-Nyquist effect, we designed a hidden stage of fast encoder measurement at 100 Hz strictly for performance measurement purposes, and then downsampled the 100 Hz measurement to 8 Hz for all the actual signal processing and filter designs.

Table 1
Experimental parameters for online signal reconstruction

Parameter	Value
Hardware	MinSegMotor (Arduino Mega 2560)
Motor	4.9 V DC motor
Encoder resolution	1336 counts/rev
Reference signal	7 Hz sinusoid, 2 V amplitude
Feedback gain	2.5×10^{-4}
Slow-sampling period T_{ss}	0.125 s (8 Hz)
Fast-sampling period T_{fs}	0.01 s (100 Hz)
Upsampling factor L	12.5
Effective sampling period T_{es}	0.005 s (200 Hz)
Run time	20 s

For brevity, we refer to W-FIR and W-IIR as the FIR- and IIR-based MMP reconstruction schemes, respectively. The slow-sampled measurements were reconstructed using the W-FIR and W-IIR and upsampled by $L = 12.5$ to $f_{fs} = 100$ Hz, followed by multi-phase reconstruction to obtain a higher effective sampling rate of $f_{es} = 200$ Hz.

Figure 7a demonstrates that both the W-FIR and W-IIR achieved comparable performance and successfully reconstructed the aliased signal. The root mean square (RMS) reconstruction error was computed after removing the aligned slow-sampled reference points and evaluating only the inter-sample reconstruction error after the transient response of the W-IIR (≈ 4 s). The signal reconstruction using W-FIR produced an RMS error of 0.093, while the W-IIR achieved an RMS error of 0.089 with $\alpha = 0.9$ in Eq. (9).

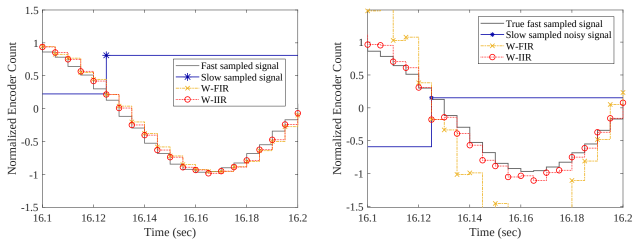

(a) (b)

Fig. 7. Comparison of signal reconstruction using W-FIR and W-IIR ($\alpha = 0.9$) for a single trial using noise-free input (subfigure a) and noisy input with an SNR of 5 dB (subfigure b).

3.4.2 *Sensitivity to Noise*

For the noise robustness study, each RMS error value was computed using a Monte Carlo average over 50 independent noise realizations. White Gaussian noise was added to the normalized fast-sampled encoder signal using MATLAB's `awgn()` function with the `'measured'` option, which computes the signal power

Table 2
RMS reconstruction error relative to W-FIR.

SNR (dB)	W-FIR RMS	W-IIR $\alpha = .3$	W-IIR $\alpha = .5$	W-IIR $\alpha = .9$
0	0.7114	0.6502	0.5523	**0.2399**
		↓8.6%	↓22.4%	**↓ 66.3%**
5	0.4008	0.3680	0.3131	**0.1435**
		↓8.2%	↓21.9%	**↓ 64.2%**
10	0.2272	0.2120	0.1821	**0.0965**
		↓6.7%	↓19.8%	**↓ 57.5%**
20	0.0919	0.0958	0.0875	**0.0714**
		↑4.2%	↓4.9%	**↓ 22.4%**
30	0.0631	0.0737	0.0701	0.0679
		↑16.8%	↑11.0%	↑7.5%

directly from the input signal before adding noise at the specified SNR. The SNR values were selected as SNR $= \{0, 3, 5, 10, 15, 20, 25, 30\}$ dB to test the robustness of the signal reconstruction using the W-IIR. For each SNR value, the slow-sampled signal was extracted from the noisy fast-sampled signal and reconstructed using the W-FIR and W-IIR. The W-IIR was evaluated for $\alpha = \{0.3, 0.5, 0.9\}$.

Figure 7b shows the reconstruction results obtained using the noisy measurements from one trial. Figure 8 shows the RMS reconstruction error using the W-FIR and W-IIR at different SNR and α values. As SNR decreases, the RMS error increases for all values of α, while larger values of α consistently reduce the reconstruction error, with the largest improvement observed in the low SNR regime and diminishing improvements beyond approximately 20 dB. A summary comparing the RMS reconstruction errors between the W-FIR and W-IIR is reported in Table 2.

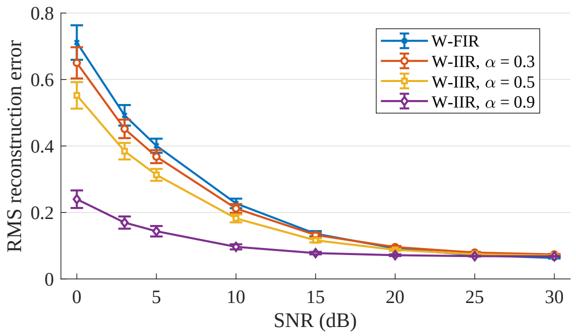

Fig. 8. RMS reconstruction error of W-FIR and W-IIR for varying α and SNR. Error bars denote one standard deviation over 50 independent noise realizations.

The improved performance of the W-IIR is attributed to the bandpass attenuation characteristics. As illustrated by the Bode plot in Fig. 9, the W-IIR behaves as a bandpass filter, allowing the target 7 Hz signal to pass while attenuating noise. However, spectral folding starting at the Nyquist frequency causes frequency components at $4(2i-1) \pm 3$ Hz and $4(2i) \pm 1$ Hz to pass, for $i \in \mathbb{Z}^+$, thereby contributing to reconstruction error. Increasing α to 1 further reduces the average error by narrowing the bandpass notch but at the cost of a slower transient response as the poles of the W-IIR approach the unit circle. This is illustrated in Fig. 10 and shown in the error plot in Fig. 11. This slower convergence contributes to the increased number of outliers observed in Fig. 12. Therefore, choice of α in the design of the W-IIR should balance trade-offs between average reconstruction error, convergence rates, and sensitivity to outliers.

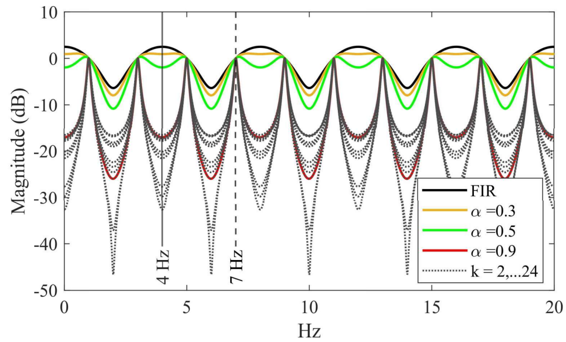

Fig. 9. Bode plots of the W-FIR and W-IIR transfer functions tuned for various bandwidths for the first inter-sample point, $k = 1$. The dotted plots denote the range of $W_{\mathrm{MMP},k}(z)$ and $\alpha = 0.9$ for inter-samples $2 \to 24$.

4 Convex Optimization Based Optimal Local-Loop Shaping

We now present the proposed optimal LLS design to reduce sensitivity amplification while preserving beyond-Nyquist disturbance rejection. To derive the objectives for optimization, we first consider the case where the feedback sampling period in Fig. 2 is uniform and fast. Figure 13 shows the resulting forward model disturbance observer structure, where the output satisfies $y[n] = y(nT_{fs})$. When no modeling error exists (i.e., $\hat{P}(z) = P(z)$), the estimated output $\hat{y}[n]$ is disturbance free, yielding $d_p[n] = y[n] - \hat{y}[n]$. In the transfer-function do-

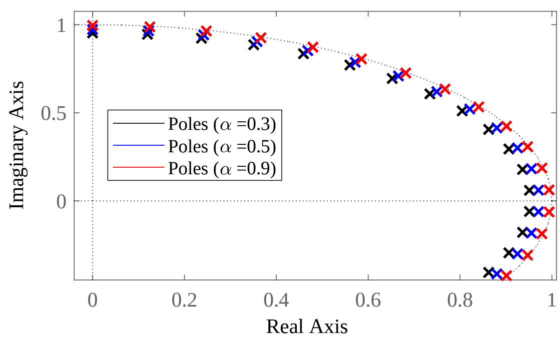

Fig. 10. Pole map of $W_{\mathrm{MMP},k}(z)$ in Eq. (10) at different α's. For the same α, $W_{MMP,k}(z)$ for each inter-sample point share the same poles.

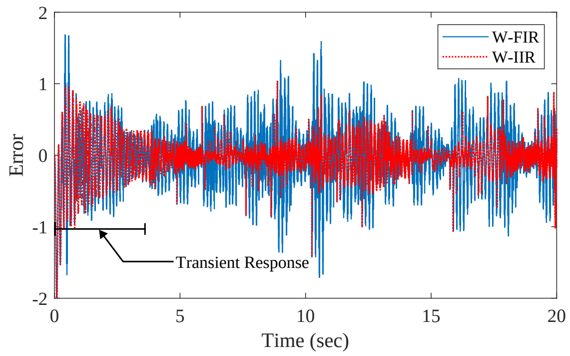

Fig. 11. Tracking error for one trial comparing W-FIR and W-IIR ($\alpha = 0.9$) based signal reconstruction.

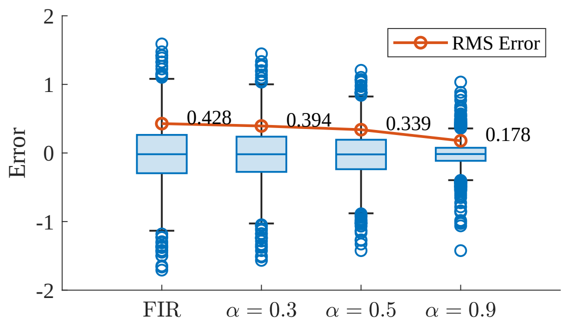

Fig. 12. Box-chart error for one trial comparing α. Reconstruction using W-FIR has 31 outliers, while reconstruction using W-IIR at $\alpha = 0.3$, 0.5 and 0.9 has 32, 43, and 134 outliers, respectively.

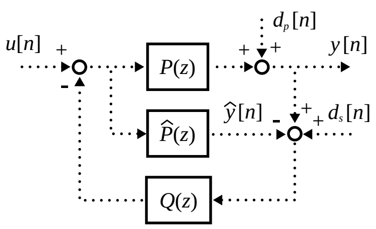

Fig. 13. Forward model DOB loop with uniform sampling.

main, we have

$$\frac{Y(z)}{D_p(z)} = 1 - \hat{P}(z)Q(z)\,. \tag{11}$$

As a special form of Youla-Kučera parameterization (see, e.g., [15]), the closed loop is stable as long as the plant and $Q(z)$ are stable.

Remark 4 *We will design $Q(z)$ to be stable; if the plant is not stable, it can be stabilized with a baseline control first and then the outer-loop structure in Fig. 3 can be implemented.*

Remark 5 *Also, it is well established (e.g., by explicitly considering the transfer function when model mismatch exists) that as long as $Q(z)$ has small enough gains at frequencies where large modeling error exists, the closed loop will also be maintained stable.*

For our focused disturbance rejection while preserving the system response to other signals, the ideal conditions are

$$1 - \hat{P}(e^{j\omega})Q(e^{j\omega}) = 0 \quad \forall \omega \in \Omega_d\,, \tag{12}$$

$$\hat{P}(e^{j\omega})Q(e^{j\omega}) = 0 \quad \forall \omega \in \Omega_{nd}\,. \tag{13}$$

where Ω_d and Ω_{nd} denote the sets of disturbance frequencies and non-disturbance frequencies, respectively, with $\Omega_d \cap \Omega_{nd} = \emptyset$. We define $\omega_{d,j}$ (rad) as the j^{th} disturbance frequency in Ω_d, and $\omega_{nd,i}$ (rad) as the i^{th} non-disturbance frequency in Ω_{nd}. Ideally, $\hat{P}(z)Q(z)$ is thus a bandpass filter that has unit gain at the disturbance frequencies and zero gain at other frequencies. Notice that the set Ω_d is finite, while Ω_{nd} is usually substantially larger and must be approximated in practice.

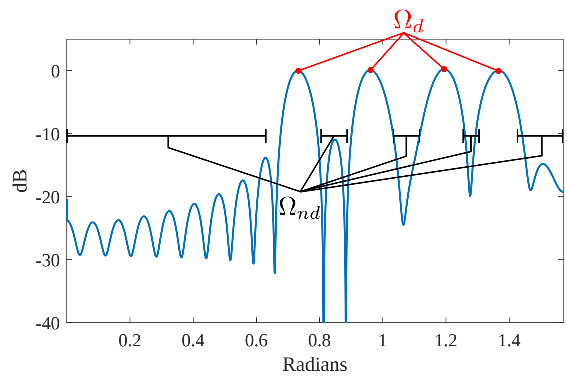

Fig. 14. Example magnitude plot of $\hat{P}(z)Q(z)$. The Q filter is parameterized such that $1 - \hat{P}(z)Q(z)$ has four attenuation notches for the disturbance frequencies. Ω_{nd} represents the non-disturbance frequency, while Ω_d has four disturbance frequencies.

Figure 14 illustrates an example of a magnitude plot of $\hat{P}(e^{j\omega})Q(e^{j\omega})$ and the corresponding regions occupied by Ω_{nd} and Ω_d. To generate attenuation notches in $1 - \hat{P}(e^{j\omega_d})Q(e^{j\omega_d})$, the product $\hat{P}(e^{j\omega_d})Q(e^{j\omega_d})$ is designed to have unit gain at the disturbance frequencies, i.e., $\hat{P}(e^{j\omega_d})Q(e^{j\omega_d}) = 1$, while remaining small over non-disturbance frequency set Ω_{nd}. In practice, we define $\Omega_{nd} = \{\omega_{nd,1}, \ldots, \omega_{nd,15r}\}$, where: 1) r is the filter order to be designed next; 2) ideally $\Omega_{nd} = [0, \pi] \backslash \{\omega_{d,j}\}$, which is approximated by discretization into $15 \times r$ frequencies following the practice in convex optimization [40]; and 3) to better capture the transition near each disturbance frequency, $\{\omega_{d,j}\}$, the nearest sampled frequencies adjacent to each disturbance frequency are placed at $\omega_{nd,i} = \omega_{d,j} - \pi/(2 \times r)$ and $\omega_{nd,i+1} = \omega_{d,j} + \pi/(2 \times r)$. This spacing may be adjusted according to the desired notch bandwidth.

We design $Q(z)$ optimally with the following structure:

$$Q(z) = Q_0(z)Q_1(z)\,, \tag{14}$$

where $Q_0(z)$ is a prescribed causal shaping filter and

$$Q_1(z) = q_0 + q_1 z^{-1} + \ldots + q_r z^{-r}$$

contains the filter coefficients $\{q_0 \ldots q_r\}$ to be solved. After subsequent formulations, such a problem falls into the category of convex optimization, and can be efficiently solved using modern tools such as CVX [14] using, e.g., the interior point method [1].

Table 3 provides a summary of different structures of $Q_0(z)$ with corresponding properties [4]. Filter selection should be based on the desired frequency behavior (e.g., low-pass, high-pass, or band-pass characteristics), and the corresponding structure is incorporated into $Q_0(z)$ to improve the reliability and conditioning of the optimization problem.

Table 3
Filter structures and properties of $Q_0(z)$

$Q_0(z)$	Type	Property
$1 - z^{-1}$	FIR	High-pass
$1 + z^{-1}$	FIR	Low-pass
$1 - \prod_{i=1}^{m} \frac{1 - 2z^{-1}\cos\omega_{d,i} + z^{-2}}{1 - 2\alpha_i z^{-1}\cos\omega_{d,i} + \alpha_i^2 z^{-2}}$	IIR	Band-pass

4.1 Design of $Q(z)$ using Second-Order Cone Programming

In this subsection, we design $Q(z)$ to achieve the desired properties in Eq. (13), prioritizing on a prescribed band-pass behavior. We formulate Eq. (13) as a quadratic constraint, allowing the problem to be solved with second-order cone programming (SOCP). To simplify notation, the prescribed filter $Q_0(z)$ is absorbed into the nominal plant model as

$$\begin{aligned} \hat{P}_0(z) &= \hat{P}(z)Q_0(z)\,, \\ &= \frac{b_{m_{P_0}} z^{m_{P_0}} + \ldots + b_1 z + b_0}{z^{n_{P_0}} + a_{n_{P_0}-1} z^{n_{P_0}-1} + \ldots + a_1 z + a_0}\,, \end{aligned} \tag{15}$$

where $n_{P_0} > m_{P_0} \geq 0$; therefore, $\hat{P}(z)Q(z) = \hat{P}_0(z)Q_1(z)$. This representation separates the fixed plant/filter dynamics from the filter parameters and allows different choices of $Q_0(z)$ to be incorporated without changing the structure of the optimization problem.

Eqs. (12) and (13) are linear for every $\omega_{d,j}$ and $\omega_{nd,i}$. To be more specific, we explicitly separate the predefined coefficients of the plant $\hat{P}(z)$ and $Q(z)$ from $\{q_0 \ldots q_r\}$, yielding

$$\hat{P}(z)Q(z) = \hat{P}_0(z)(q_0 + q_1 z^{-1} + \ldots + q_r z^{-r})\,, \tag{16}$$
$$= \hat{P}_0(z) q^T \phi(z)\,, \tag{17}$$

with $\phi(z) = \begin{bmatrix} 1, & z^{-1}, & \cdots & z^{-r} \end{bmatrix}^T$ and

$$q = \begin{bmatrix} q_0, & q_1, & \cdots & q_r \end{bmatrix}^T .$$

Substituting in $z = e^{j\omega}$, Eq. (17) is divided into real and imaginary components such that

$$\hat{P}_0(e^{j\omega}) q^T \phi(e^{j\omega}) = \left[\hat{P}_{0,R}(e^{j\omega}) + j\hat{P}_{0,I}(e^{j\omega})\right] q^T \left[\phi_R(e^{j\omega}) - j\phi_I(e^{j\omega})\right]\,, \tag{18}$$

where we have represented the plant as its real and imaginary components $\hat{P}_0 = \hat{P}_{0,R} + j\hat{P}_{0,I}$ (the term $e^{j\omega}$ is omitted here and forward for brevity), and

$$\phi_R(e^{j\omega}) = \begin{bmatrix} 1, & \cos(\omega), & \cdots & \cos(r\omega) \end{bmatrix}^T ,$$
$$\phi_I(e^{j\omega}) = \begin{bmatrix} 0, & \sin(\omega), & \cdots & \sin(r\omega) \end{bmatrix}^T .$$

Substituting Eq. (18) into Eq. (12) yields

$$q^T\left(\hat{P}_{0,R}\phi_R + \hat{P}_{0,I}\phi_I\right) + jq^T\left(\hat{P}_{0,I}\phi_R - \hat{P}_{0,R}\phi_I\right) = 1\,. \tag{19}$$

Equation (19) is an exact constraint equivalent to Eq. (12). It is linear and convex with respect to q.

Regarding the other design property of Eq. (13), as it is not feasible to have zero magnitude for the entire non-disturbance frequencies, we relax it to a magnitude constraint of $|\hat{P}(e^{j\omega})Q(e^{j\omega})| \leq \epsilon(\omega)$. Taking the square removes the imaginary term and yields

$$\begin{aligned} q^T\Big[&\phi_R(e^{j\omega})|\hat{P}_0(e^{j\omega})|^2 \phi_R^T(e^{j\omega}) \\ &+ \phi_I(e^{j\omega})|\hat{P}_0(e^{j\omega})|^2 \phi_I^T(e^{j\omega})\Big] q \leq \rho(\omega), \end{aligned} \tag{20}$$

where $|\hat{P}_0(\cdot)|^2 = \hat{P}_{0,R}^2(\cdot) + \hat{P}_{0,I}^2(\cdot)$ and $\rho(\cdot) = \epsilon(\cdot)^2$. Equation (20) is a quadratic inequality at one non-disturbance frequency. If the size of Ω_{nd} is n_m, we form n_m such inequalities.

Integrating both the bandstop and bandpass signal criteria, the proposed SOCP for optimal LLS is

$$\begin{aligned} &\min_{\rho,q} \sum_{i=1}^{n_m} \rho(\omega_{nd,i}) \qquad (21)\\ &\text{subject to } 1-\hat{P}_0(e^{j\omega_{d,i}})\phi^T(e^{j\omega_{d,i}})q = 0 \quad \forall i = 1,\ldots,m\\ &\qquad q^T\Big[\phi_R(e^{j\omega_{nd,i}})|\hat{P}_0(e^{j\omega_{nd,i}})|^2\phi_R^T(e^{j\omega_{nd,i}}) + \ldots\\ &\qquad\quad \phi_I(e^{j\omega_{nd,i}})|\hat{P}_0(e^{j\omega_{nd,i}})|^2\phi_I^T(e^{j\omega_{nd,i}})\Big]q\\ &\qquad \leq \rho(\omega_{nd,i})\ \forall i = 1,\ldots,n_m \end{aligned}$$

This formulation has several advantages. First, relaxing the constraint in Eq. (20) yields a feasible solution, allowing standard SOCP solvers to efficiently identify optimal filter parameter. Second, the minimum bound $\rho(\omega_{nd,i})$ is determined directly through optimization, enabling the designer to focus on specifying the frequency regions of interest rather than prescribing exact magnitude levels. As a result, there is greater flexibility in tuning the filter based on desired frequency regions.

Remark 6 *The SOCP provides exact disturbance rejection at $\omega_{d,i}$ $\forall i \in (1, m)$. If only partial disturbance attenuation is desired in practice, a positive scaling factor $\zeta[\in (0, 1)]$ can be added such that $Q \to \zeta Q$. If a more prescribed attenuation depth profile is desired, the first linear constraint can also be flexibly adjusted, e.g., to $\zeta_i - \hat{P}_0(e^{j\omega_{d,i}})\phi^T(e^{j\omega_{d,i}})q = 0 \quad \forall i = 1,\ldots,m$, and $0 < \zeta_i \leq 1$.*

4.2 Design of $Q(z)$ Via Semi-Definite Programming

We have applied SOCP for solving a feasible bound for the bandpass constraint in Eq. (20). However, the SOCP does not directly minimize amplifications in Eq. (11) rooted in the celebrated Bode's Integral Theorem. To address this, we formulate the objective function to minimize the H_∞–norm (maximum magnitude response) of Eq. (11), using a special form of the discrete-time Bounded-Real lemma [23, 24], which transforms a bounded-input bounded-output (BIBO) stable discrete-time LTI system $G(z)$'s infinity norm inequality $\|G(z)\|_\infty \leq \gamma$ to the existence of a positive semi-definite matrix M such that a matrix inequality holds:

$$\begin{bmatrix} M & MA_d & MB_d & \mathbf{0}\\ A_d^TM & M & \mathbf{0} & C_d^T\\ B_d^TM & \mathbf{0} & \gamma\mathbf{I} & D_d^T\\ \mathbf{0} & C_d & D_d & \gamma\mathbf{I} \end{bmatrix} \preceq 0. \qquad (22)$$

Any state-space representation of the Bounded-Real Lemma (see, e.g., [3]) can be used so long as linearity with respect to q and M is preserved in the matrix inequality. In the proposed formulation, we design to transform Eq. (11) into its controllable canonical form (CCF), which stores the coefficients of $Q_1(z)$—q (in vector form)—in matrices C_d and D_d. As a result, the matrix inequality in Eq. (22) becomes linear in terms of both q and M, preserving convexity. We then formulate the filter as a semi-definite programming (SDP) problem. Specifically, given the discrete-time system represented by Eq. (15), we choose the state-space representation in the CCF:

$$\begin{aligned} x_{\hat{P}_0}[n+1] &= A_{\hat{P}_0}x_{\hat{P}_0}[n] + B_{\hat{P}_0}u[n]\,,\\ y_{\hat{P}_0}[n] &= C_{\hat{P}_0}x_{\hat{P}_0}[n] + D_{\hat{P}_0}u[n]\,, \end{aligned} \qquad (23)$$

with

$$A_{\hat{P}_0} = \begin{bmatrix} 0 & 1 & \cdots & 0\\ \vdots & \vdots & \ddots & \vdots\\ 0 & 0 & \cdots & 1\\ -a_0 & -a_1 & \cdots & -a_{n_{P_0}-1} \end{bmatrix}, \qquad B_{\hat{P}_0} = \begin{bmatrix} 0\\ \vdots\\ 0\\ 1 \end{bmatrix},$$

$$C_{\hat{P}_0} = \begin{bmatrix} b_0, & \cdots & b_{m_{P_0}}, & \mathbf{0_{1x(n_{P_0}-m_{P_0}-1)}} \end{bmatrix}, \quad D_{\hat{P}_0} = [0]\,.$$

Note that the input for $Q_1(z)$ is the output of $\hat{P}_0(z)$. Then, the state-space representation of Eq. (14) in CCF is

$$\begin{aligned} x_{Q_1}[n+1] &= A_{Q_1}x_{Q_1}[n] + B_{Q_1}y_{\hat{P}_0}[n]\,,\\ y_{Q_1}[n] &= C_{Q_1}x_{Q_1}[n] + D_{Q_1}y_{\hat{P}_0}[n]\,, \end{aligned} \qquad (24)$$

with

$$A_{Q_1} = \begin{bmatrix} 0 & 1 & \cdots & 0\\ \vdots & \vdots & \ddots & \vdots\\ 0 & 0 & \cdots & 1\\ 0 & 0 & \cdots & 0 \end{bmatrix}, \quad B_{Q_1} = \begin{bmatrix} 0\\ \vdots\\ 0\\ 1 \end{bmatrix},$$

$$C_{Q_1} = \begin{bmatrix} q_r, & \cdots & q_1 \end{bmatrix}, \quad D_{Q_1} = [q_0]\,.$$

Let the state variable be $\hat{x}[n] = \begin{bmatrix} x_{\hat{P}_0}^T[n] & x_{Q_1}^T[n] \end{bmatrix}^T$. The state-space representation of Eq. (11) is

$$\begin{aligned} \hat{x}[n+1] &= \hat{A}\hat{x}[n] + \hat{B}u[n]\,,\\ \hat{y}[n] &= \hat{C}\hat{x}[n] + \hat{D}u[n]\,, \end{aligned} \qquad (25)$$

with

$$\hat{A} = \begin{bmatrix} A_{\hat{P}_0} & \mathbf{0_{n_{P_0}\times r}}\\ B_{Q_1}C_{\hat{P}_0} & A_{Q_1} \end{bmatrix}, \quad \hat{B} = \begin{bmatrix} B_{\hat{P}_0}\\ B_{Q_1}D_{\hat{P}_0} \end{bmatrix},$$

$$\hat{C} = -\begin{bmatrix} D_{Q_1}C_{\hat{P}_0} & C_{Q_1} \end{bmatrix}, \quad \hat{D} = [1 - D_{Q_1}D_{\hat{P}_0}]\,.$$

We apply the discrete-time Bounded-Real Lemma from Eq. (22) to the state-space in Eq. (25) and have the minimization problem for the SDP filter:

$$
\begin{aligned}
&\min_{\gamma,q,M} \quad \gamma && (26)\\
&\text{subject to} \quad 1-\hat{P}_0(e^{j\omega_{d,j}})\phi^T(e^{j\omega_{d,j}})q=0 \quad \forall j=1,\dots,m\\
&\qquad \begin{bmatrix} M & M\hat{A} & M\hat{B} & \mathbf{0}\\ \hat{A}^T M & M & \mathbf{0} & \hat{C}^T\\ \hat{B}^T M & \mathbf{0} & \gamma\mathbf{I} & \hat{D}^T\\ \mathbf{0} & \hat{C} & \hat{D} & \gamma\mathbf{I}\end{bmatrix} \preceq 0\\
&\qquad M\succeq 0,\ \gamma\geq 0\\
&\qquad q^T\Big[\phi_R(e^{j\omega_{nd,i}})|\hat{P}_0(e^{j\omega_{nd,i}})|^2\phi_R^T(e^{j\omega_{nd,i}})+\dots\\
&\qquad\quad \phi_I(e^{j\omega_{nd,i}})|\hat{P}_0(e^{j\omega_{nd,i}})|^2\phi_I^T(e^{j\omega_{nd,i}})\Big]q\\
&\qquad \leq \rho(\omega_{nd,i})\ \forall i=1,\dots,n_m
\end{aligned}
$$

Here, $\rho(\cdot)$ becomes a tunable design parameter specified prior to optimization and determines the allowable frequency-dependent bound in the quadratic constraint to enforce bandpass characteristics over selected frequency regions.

Similar as before, when $Q_0(z)=1$, $1-z^{-1}$, or $1+z^{-1}$ in Eq. (14), the resulting Q filter will be an FIR filter. If $Q_0(z)$ is a bandpass filter as specified in Table 3, the final Q filter $Q(z)=Q_0(z)Q_1(z)$ will be an IIR filter. We use the terms SDP-FIR and SDP-IIR to refer to $Q(z)$ filters designed using SDP with FIR and IIR parameterizations, respectively.

Also, analogous to Remark 6, additional scaling can be applied in the first equality constraint to further fine tune the Q profile.

5 Verification and Experimental Results

5.1 Configuration and Baseline Performance

Simulations were conducted in MATLAB/Simulink using the in-house SLS machine model shown in Fig. 1a. The nominal closed-loop laser scanner model is [19]

$$\tilde{P}(z)=\frac{0.0282z^2+0.1504z+0.1146}{z^4-1.3190z^3+0.9290z^2-0.6073z-0.0035}\,.$$

Since a vendor-integrated baseline controller is embedded in the plant, we implement the MFMDOB using the structure in Fig. 3, with $r[n]=0$. The main simulation parameters are summarized in Table 4, with the filter order selected as $r=30$. Beyond this order, the SDP optimal value exhibited diminishing improvement, as discussed in Sec. 5.2. The SOCP and SDP-FIR designs use the high-pass $Q_0(z)$ structure in Table 3, whereas the SDP-IIR design uses the band-pass $Q_0(z)$ structure.

Table 4
Simulation parameters for numerical verification

Parameter	Value
System model	SLS laser scanner [19]
Fast-sampling period, T_{fs}	2.5×10^{-5} s (40 kHz)
Slow-sampling period, T_{ss}	6.25×10^{-5} s (16 kHz)
Nyquist frequency, f_N	8 kHz
Sampling ratio, L	2.5
NMP zero	$z=-4.419$
Filter order, r	30
Disturbance frequencies	9.360, 12.328, 15.064, 17.464 kHz
Normalized frequencies	1.170, 1.541, 1.883, 2.183 f_N
Disturbance amplitudes	0.555, 0.121, 0.451, 0.7159
Plant/sensor noise	Unity-power WGN
Reconstruction	W-FIR and W-IIR
$Q(z)$ designs	SOCP, SDP-FIR, SDP-IIR, and bandpass [19]
IIR parameter, α	0.9 (W-IIR and SDP-IIR)
Platform	MATLAB/Simulink

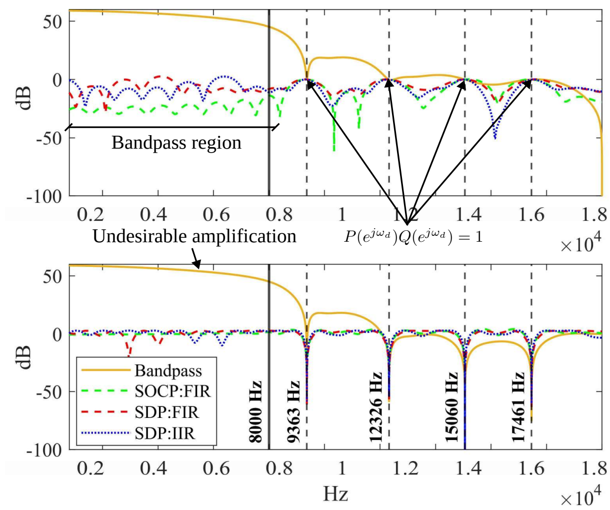

Fig. 15. Bode plots of $\hat{P}(z)Q(z)$ (top) and $1-\hat{P}(z)Q(z)$ (bottom). The Nyquist frequency is 8000 Hz, and the four disturbances are indicated by the dashed lines. The optimization yielded successful Q filters using SOCP and SDP, with deep attenuation notches for the beyond-Nyquist disturbances.

Figure 15 shows the Bode plots of $\hat{P}(z)Q(z)$ and $1-\hat{P}(z)Q(z)$ for the bandpass, SOCP and SDP parameterizations. At the disturbance frequencies, the designed filters satisfy $\hat{P}(e^{j\omega_d})Q(e^{j\omega_d})\approx 1$, producing attenuation notches for the disturbance frequencies in $1-\hat{P}(e^{j\omega_d})Q(e^{j\omega_d})$. Away from the disturbance frequencies, SOCP and SDP designs reduce the magnitude of $\hat{P}(e^{j\omega})Q(e^{j\omega})$, thereby limiting unnecessary ampli-

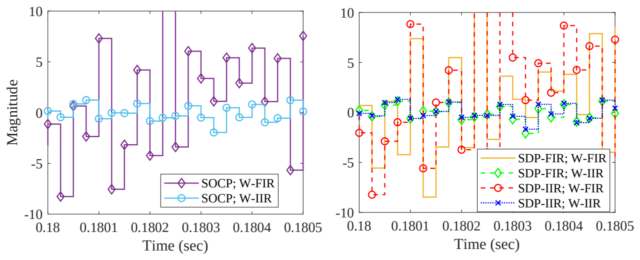

(a) (b)

Fig. 16. Output response of the system at the fast-sampling period T_{fs} for (a) SOCP parameterized filters and (b) SDP parameterized filters using W-FIR and W-IIR signal reconstruction. The output of the baseline bandpass $Q(z)$ filter is omitted because it became unstable. The desired output is $y[n] = 0$.

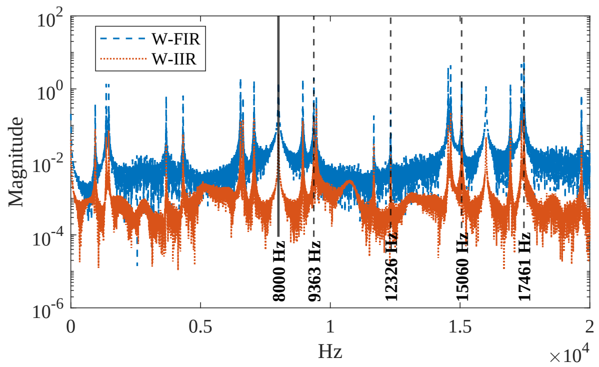

Fig. 17. Spectral plot of the reconstructed fast disturbance beyond-Nyquist frequency using W-FIR and W-IIR.

fication at non-disturbance frequencies. The SOCP design yields the smallest response over the specified non-disturbance region because it directly constrains the frequency-dependent bound $\rho(\Omega_{nd})$ in Eq. (21). In contrast, the baseline bandpass design exhibits larger amplification below the Nyquist frequency, reflecting the waterbed-type trade-off associated with wider beyond-Nyquist attenuation notches.

Figure 16 shows the system outputs obtained using different $Q(z)$ designs with W-FIR and W-IIR signal reconstruction. The output using the baseline bandpass filter became unstable due to noise amplification and is therefore omitted. The results show that the signal reconstruction stage significantly reduces noise sensitivity. At the disturbance frequencies, both the W-FIR and W-IIR preserve the components required for signal reconstruction. However, the W-IIR behaves as a bandpass filter by attenuating non-disturbance frequencies, which improves reconstruction accuracy, consistent with noisy-signal validation in Sec. 3.4.2. This behavior is also observed in the spectral comparison in Fig. 17, where the W-IIR reduces non-disturbance spectral components relative to W-FIR. The RMS errors are summarized in Table 5, where W-IIR reduces the RMS error by more than 90% for all optimized $Q(z)$ designs.

Table 5
RMS error for W-FIR and W-IIR with different $Q(z)$ designs.

Method	**Bandpass**	**SOCP**	**SDP-FIR**	**SDP-IIR**
W-FIR	Unstable	8.965	8.588	9.631
W-IIR	Unstable	**0.849**	**0.852**	**0.841**
Change	–	↓ **90.5%**	↓ **90.1%**	↓ **91.3%**

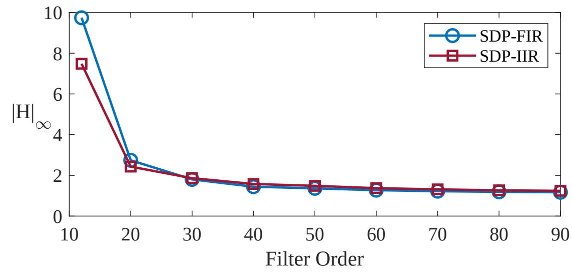

Fig. 18. Comparison of the optimal value of the SDP-FIR and SDP-IIR filters at various filter orders.

5.2 Optimal Value

Figure 18 shows the optimal value of the objective function in Eq. (26), corresponding to the H_∞ norm of $1 - \hat{P}(z)Q(z)$, for different Q filter orders using the SDP-FIR and SDP-IIR filter parameterizations. The SDP-IIR filter achieves lower optimal values up to approximately $r = 30$, indicating a a smaller upper bound on the worse-case magnitude of $1 - \hat{P}(z)Q(z)$ across the frequency spectrum. Beyond $r \approx 30$, the improvement becomes marginal, suggesting that increasing the filter order provides limited additional benefit in local-loop shaping performance.

The SDP-IIR filter also provides an additional degree of design flexibility through the parameter, α, which controls the effective bandwidth and notch characteristics. As shown in Fig. 19, increasing α toward unity narrows the bandwidth and increases the notch attenuation at the disturbance frequencies. It also improves the bandpass characteristics between disturbance frequencies, particularly for $\alpha = 0.99$. However, as α approaches 1, the poles of the SDP-IIR filter move closer to the unit circle, increasing the transient response time of the filter.

The SOCP and SDP parameterized filters show similar disturbance-rejection behavior in Fig. 15; however, the SDP objective function provides a more interpretable optimal value. Specifically, the SDP minimizes $\|1 - \hat{P}(z)Q(z)\|_\infty$, which represents the maximum magnitude of the added error-rejection transfer function over frequency. In contrast, the SOCP objective $\sum_i \rho(\omega_{nd,i})$ is a gridded aggregate bound over the non-disturbance frequencies and is less directly interpretable as a closed-loop performance metric.

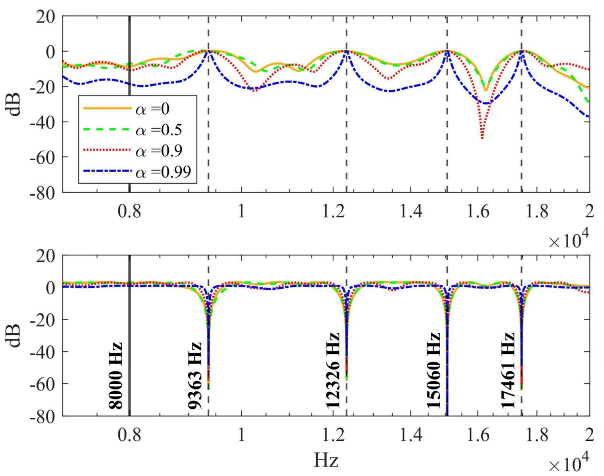

Fig. 19. Bode plot of $P(z)Q(z)$ (top) and $1-P(z)Q(z)$ (bottom) using the SDP-IIR filter at different α's.

5.3 *Robustness*

This subsection evaluates the robustness of the proposed MFMDOB using the special implementation in Fig 3. Transfer-function analysis yields

$$\begin{aligned} Y(z) =& \tilde{P}(z)R(z) + \left(1-\bar{P}(z)Q(z)W_{\mathrm{MMP},k}(z)\right)D_p(z) \\ &- \tilde{P}(z)Q(z)W_{\mathrm{MMP},k}(z)D_s(z), \end{aligned} \tag{27}$$

where

$$\tilde{P}(z) = \frac{P(z)C(z)}{1+P(z)C(z)},$$

denotes the closed-loop plant obtained from the ZOH-discretized plant $P(z)$ and baseline controller $C(z)$. Under the assumptions of nominal-model match $\hat{P}(z) = \tilde{P}(z)$ and uniform fast-sampling in the closed loop, the corresponding disturbance sensitivity and complementary disturbance sensitivity functions are

$$S(z) = 1 - \tilde{P}(z)Q(z)W_{\mathrm{MMP},k}(z), \tag{28}$$
$$T(z) = \tilde{P}(z)Q(z)W_{\mathrm{MMP},k}(z), \tag{29}$$

or equivalently,

$$S(z) = \frac{1+P(z)C(z)\left(1-Q(z)W_{\mathrm{MMP},k}(z)\right)}{1+P(z)C(z)}, \tag{30}$$
$$T(z) = \frac{P(z)C(z)Q(z)W_{\mathrm{MMP},k}(z)}{1+P(z)C(z)}. \tag{31}$$

Thus, the zeros of $T(z)$ include contributions from $P(z)$, $C(z)$, $Q(z)$, and $W_{\mathrm{MMP},k}(z)$.

We consider stability when the plant is perturbed to $P(e^{j\omega}) \to P(e^{j\omega})(1+\beta(e^{j\omega})\Delta)$, where $|\beta(e^{j\omega})|$ is the magnitude of the uncertainty and Δ is a stable, unity-H_∞–norm bounded uncertainty. Applying the Small Gain Theorem gives the following robust-stability condition [29]:

$$|T(e^{j\omega})\beta(e^{j\omega})| < 1 \quad \forall\omega, \tag{32}$$

which requires the uncertainty magnitude $\beta(e^{j\omega})$ to remain below the magnitude of the inverse complementary transfer function $1/|T(e^{j\omega})|$. Ideally, this translates to a desire for $\|T(z)\|_\infty$ to be small. However, from Bode's Integral Theorem, we have [35]

$$\int_0^{2\pi} \ln|S(e^{j\omega})|d\omega = 2\pi \cdot \sum \ln|p_i|, \tag{33}$$
$$\int_0^{2\pi} \ln|T(e^{j\omega})|d\omega = 2\pi \cdot \sum \ln|z_i|, \tag{34}$$

where p_i denote equivalent open-loop unstable poles, and z_i denote the equivalent open-loop NMP zeros. The equivalent open loop here refers to the transfer function $L(z)$ such that $1/(1+L(z))$ yields the sensitivity function in Eq. (30). When nonminimum-phase zeros are present, Eq. (34) implies that reducing $|T(e^{j\omega})|$ over selected frequency regions generally requires amplification elsewhere. As the number or magnitude of NMP zeros increases, unavoidable peaks appear in the complementary sensitivity transfer function, and the lower bound on $\|T(z)\|_\infty$ increases with $\sum\ln|z_i|$. Consequently, our objective is to minimize them through appropriate design of $Q(z)$, where convex optimization is useful for minimizing sensitivity amplifications.

Table 6
Magnitude of $1/|T(z)|$ at the disturbance frequencies.

Method	f (Hz)	W-FIR	W-IIR	Change
SOCP	9363	1.207	1.207	–
	12326	1.077	1.080	↑ 0.32%
	15060	0.966	1.928	↑ 99.7%
	17461	0.979	0.064	↓ 93.4%
SDP-FIR	9363	1.207	1.207	–
	12326	1.077	1.076	↓ 0.05%
	15060	0.966	0.774	↓ 19.8%
	17461	0.979	0.035	↓ 96.5%
SDP-IIR	9363	1.207	1.207	–
	12326	1.077	1.077	–
	15060	0.966	0.966	–
	17461	0.979	0.981	↑ 0.21%

Figure 20 compares the inverse complementary sensitivity $1/T(z)$ for the W-FIR and W-IIR formulations, and Table 6 summarizes its magnitudes at the disturbance frequencies. Robust stability is guaranteed when the uncertainty weight in Eq. (32) remains below $1/|T(e^{j\omega})|$ over the frequency range. Figure 20a shows that W-FIR produces multiple dips of $1/|T(z)|$ below -20 dB, indicating reduced robustness margins across several frequency regions. In these regions, multiplicative plant uncertainty greater than approximately 10%

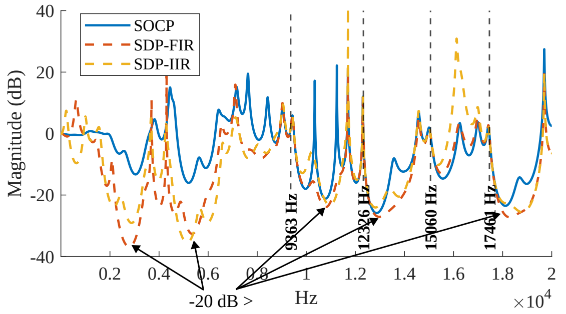

(a)

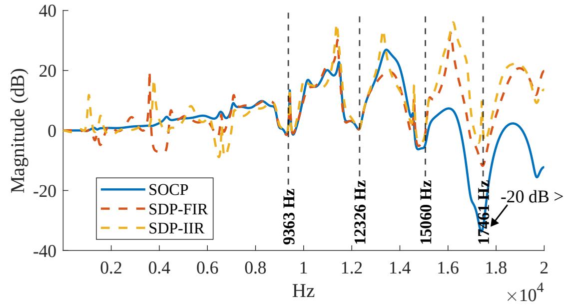

(b)

Fig. 20. Bode plots of $1/T(z)$ using (a) W-FIR (b) W-IIR.

may compromise robust stability. In contrast, Fig. 20b shows that W-IIR concentrates the reduction in robustness margin primarily near the disturbance frequency of 17461 Hz while maintaining larger values of $1/|T(z)|$ elsewhere. This indicates that W-IIR localizes the robustness trade-off near the target disturbance frequency instead of spreading sensitivity degradation over a wider bandwidth. Summing up, the SDP-IIR filter design combined with W-IIR improves reconstruction accuracy while maintaining favorable robustness margins without requiring substantially higher filter order.

6 Conclusion

We proposed an optimally designed MFMDOB for attenuating structured disturbances beyond the Nyquist frequency of the feedback sensor for NMP systems. To enable beyond-Nyquist disturbances under fractional multirate sampling relationships, we introduced a MMP capable of reconstructing fast-rate signals from sparely aligned slow-sampled measurements. The disturbance observer filter $Q(z)$ was formulated using convex frequency-domain constraints and solved through SOCP and SDP to achieve robust LLS and improved noise attenuation. Hardware testing validated the effectiveness of non-integer signal reconstruction using both W-FIR and W-IIR, while demonstrating improved reconstruction accuracy of the W-IIR under noisy conditions. Simulations conducted on the in-house SLS system, a NMP system, further verified that the proposed MFMDOB improves robustness to measurement noise and enhances stability margins under model uncertainty. Overall, the proposed MFMDOB provides novel beyond-Nyquist disturbance rejection for fractional multirate systems while preserving robust closed-loop performance.

Acknowledgment

This material is based upon work supported by the U.S. National Science Foundation under Grant No. 2141293. Any opinions, findings, and conclusions, or recommendations expressed in this material are those of the author(s) and do not necessarily reflect the views of the National Science Foundation.

A Multirate Model Predictor Derivation for Non-Integer Sampling Period Ratios

Signal reconstruction in Eq. (8) is feasible when the Internal Model $A_d(z^{-1})d[n] \to 0$ holds (see Eq. (5)).

We construct a special Diophantine equation:

$$F(z^{-1})A(z^{-1}) + z^{-k}W_k(z^{-N_L}) - B^*(z^{-N_L}) = 1\,, \tag{A.1}$$

with

$$\begin{aligned}
F(z^{-1}) =& 1 + \sum_{i=1}^{2m(N_L-1)} f_{k,i} z^{-i}\,,\\
W_k(z^{-N_L}) =& \sum_{i=0}^{n_w} w_{k,i} z^{-iN_L}\,,\\
B^*(z^{-N_L}) =& -1 + \prod_{i=1}^{m} \big(1 - 2\alpha\cos(2\pi N_L T_{fs} f_{d,i}) z^{-N_L}\\
& \ldots + \alpha^2 z^{-2N_L}\big)\,,\\
\triangleq & \sum_{i=1}^{2m} b_i z^{-iN_L}\,.
\end{aligned}$$

Note how we designed the order of z^{-1} in W_k and B^* to contain only integer multiples of N_L for picking the sparse sampled signals.

The coefficients of $W_k(z^{-N_L})$ can be solved by matching the powers of z^{-i} in Eq. (A.1), leading to the linear system:

$$
M_k \begin{bmatrix} f_{k,1} \\ \vdots \\ f_{k,2m(N_L-1)} \\ w_{k,0} \\ \vdots \\ w_{k,n_w} \end{bmatrix} = \begin{bmatrix} -a_1 \\ -a_2 \\ \vdots \\ -a_{2m} \\ 0 \\ \vdots \\ 0 \end{bmatrix} + \begin{bmatrix} \mathbf{0_{(N_L-1)\times 1}} \\ b_1 \\ \mathbf{0_{(N_L-1)\times 1}} \\ b_2 \\ \vdots \\ b_m \\ \vdots \end{bmatrix} . \tag{A.2}
$$

where $M_k \in \mathbb{R}^{2mN_L \times 2mN_L}$ is defined as

$$
M_k \triangleq \left[\tilde{M}_k \mid e_k,\ e_{k+N_L},\ \cdots\ e_{k+(2m-1)N_L} \right] , \tag{A.3}
$$

$\tilde{M}_k \in \mathbb{R}^{2mN_L \times 2m(N_L-1)}$ is a Toeplitz block:

$$
\tilde{M}_k \triangleq \begin{bmatrix} 1 & \cdots & 0 \\ \vdots & \ddots & \vdots \\ a_{2m} & \ddots & 1 \\ \vdots & \ddots & \vdots \\ 0 & \cdots & a_{2m} \end{bmatrix} ,
$$

and e_i denotes the standard basis vector having one in the i^{th} row and zeros elsewhere.

The minimum-order solution exists when M_k is full row rank, i.e. $n_w = 2m - 1$. Using the result of Eq. (5), we multiply the Diophantine equation in Eq. (A.1) by $d_{fs}[n]$ and apply the delay shift z^{-k}. At steady state, we obtain

$$
d_{fs}[n] = W_k(z^{-N_L}) d_{fs}[n-k] + B^*(z^{-N_L}) d_{fs}[n] . \tag{A.4}
$$

Equation (A.4) expands as a weighted sum of the coefficients of $W_k(z^{-N_L})$ and $B^*(z^{-N_L})$. Evaluating at $n = nN_L + k$ yields

$$
\begin{aligned}
d_{fs}[nN_L + k] =& w_{k,0} d_{fs}[nN_L] + \dots \\
& + w_{k,n_w} d_{fs}[(n - n_w)N_L] \\
& - b_1 d_{fs}[(n-1)N_L + k] - \dots \\
& - b_{2m} d_{fs}[(n-2m)N_L + k] .
\end{aligned} \tag{A.5}
$$

Equation (A.5) shows that the k^{th} inter-sample point is expressed as a weighted sum of historical fast-sampled measurements, where the weights given by the coefficients of $W_k(z^{-N_L})$ are equivalent to those associated with the slow-sampled measurements defined in Eq. (2). Using this relation, Eq. (A.5) can be equivalently expressed as

$$
\begin{aligned}
d_{fs}[nN_L + k] =& w_{k,0} d_{ss}[D_L n] + \dots \\
& + w_{k,n_w} d_{ss}[D_L(n - n_w)] - \dots \\
& - b_1 d_{fs}[(n-1)N_L + k] - \dots \\
& - b_{2m} d_{fs}[(n-2m)N_L + k] .
\end{aligned} \tag{A.6}
$$

Thus Eq. (A.6) provides the estimate of the k^{th} inter-sample between $d_{fs}[N_L n]$ and $d_{fs}[N_L(n+1)]$.

References

[1] F. Alizadeh and D. Goldfarb. Second-order cone programming. *Mathematical Programming*, 95:3–51, 2003.

[2] Saeid Bashash and Shahriar Shariat. Performance enhancement of hard disk drives through data-driven control design and population clustering. *Precision Engineering*, 56:267–279, 2019.

[3] Ryan James Caverly and James Richard Forbes. LMI properties and applications in systems, stability, and control theory. *CoRR*, abs/1903.08599, 2019.

[4] Xu Chen, Tianyu Jiang, and Masayoshi Tomizuka. Pseudo youla–kucera parameterization with control of the waterbed effect for local loop shaping. *Automatica*, 62:177–183, 2015.

[5] Xu Chen and Masayoshi Tomizuka. A minimum parameter adaptive approach for rejecting multiple narrow-band disturbances with application to hard disk drives. *IEEE Transactions on Control Systems Technology*, 20(2):408–415, 03 2012.

[6] Xu Chen and Masayoshi Tomizuka. Optimal decoupled disturbance observers for dual-input single-output systems. *Journal of Dynamic Systems, Measurement, and Control*, 136(5):051018, 07 2014.

[7] Xu Chen and Masayoshi Tomizuka. Overview and new results in disturbance observer based adaptive vibration rejection with application to advanced manufacturing. *International Journal of Adaptive Control and Signal Processing*, 29:1459–1474, 2015.

[8] Xu Chen and Masayoshi Tomizuka. Discrete-time reduced-complexity youla parameterization for dual-input single-output systems. *IEEE Transactions on Control Systems Technology*, 24(1):302–309, 2016.

[9] Xu Chen and Hui Xiao. Multirate forward-model disturbance observer for feedback regulation beyond nyquist frequency. *Systems and Control Letters*, 94:181–188, 2016.

[10] Regev Cohen and Yonina C. Eldar. Sparse doppler sensing based on nested arrays. *IEEE Transactions on Ultrasonics, Ferroelectrics, and Frequency Control*, 65(12):2349–2364, 2018.

[11] P.I. Corke and M.C. Good. Dynamic effects in visual closed-loop systems. *IEEE Transactions on Robotics and Automation*, 12(5):671–683, 1996.

[12] G. F. Franklin, J. D. Powell, and A. Emami-Naeini. *Feedback Control of Dynamic Systems*. Pearson, 7 edition, 2015.

[13] H. Fujimoto and Y. Hori. Vibration suppression and optimal repetitive disturbance rejection control in semi-nyquist frequency region using multirate sampling control. In *Proceedings of the 39th IEEE Conference on Decision and Control*, volume 4, pages 3745–3750 vol.4, 2000.

[14] Michael Grant and Stephen Boyd. CVX: Matlab software for disciplined convex programming, version 2.2. `http://cvxr.com/cvx`, 2020.

[15] Erik Hedberg, Johan Löfberg, and Anders Helmersson. A pedagogical path from the internal model principle to youla-kučera parametrization. *IFAC-PapersOnLine*, 53(2):17374–17379, 2020. 21st IFAC World Congress.

[16] Xiaohai Hu, Thomas L Chu, and Xu Chen. State-space system identification beyond the nyquist frequency with collaborative non-uniform sensing data. In *2024 American Control Conference (ACC)*, pages 5400–5405. IEEE, 2024.

[17] Qing-Wei Jia. Disturbance rejection through disturbance observer with adaptive frequency estimation. *Magnetics, IEEE Transactions on*, 45:2675 – 2678, 07 2009.

[18] Tianyu Jiang, Jiong Tang, and Xu Chen. Wide-band loop shaping for modulation of energy transmission in nonminimum-phase systems. In *Proceedings of ASME Dynamic Systems and Control Conference*, page V002T18A001, 10 2018.

[19] Tianyu Jiang, Hui Xiao, Jiong Tang, Liting Sun, and Xu Chen. Local loop shaping for rejecting band-limited disturbances in nonminimum-phase systems with application to laser beam steering for additive manufacturing. *IEEE Transactions on Control Systems Technology*, 28:2249–2262, 11 2020.

[20] Jinbum Kang, Heechul Yoon, Changhan Yoon, and Stanislav Y. Emelianov. High-frequency ultrasound imaging with sub-nyquist sampling. *IEEE Transactions on Ultrasonics, Ferroelectrics, and Frequency Control*, 69(6):2001–2009, 2022.

[21] Kenta Koiwa, Toru Kuribayashi, Tadanao Zanma, Kang-Zhi Liu, Kenji Natori, and Yukihiko Sato. Stability and robust performance analysis of grid-connected inverter with high-order filter: Resonances beyond the nyquist frequency. *IET Control Theory & Applications*, 15(14):1818–1831, 2021.

[22] Ioan Doré Landau, Abraham Castellanos Silva, Tudor-Bogdan Airimitoaie, Gabriel Buche, and Mathieu Noe. Benchmark on adaptive regulation—rejection of unknown/time-varying multiple narrow band disturbances. *European Journal of Control*, 19(4):237–252, 2013.

[23] I. Masubuchi, A. Ohara, and N. Suda. Lmi-based output feedback controller design-using a convex parametrization of full-order controllers. In *Proceedings of 1995 American Control Conference - ACC'95*, volume 5, pages 3473–3477 vol.5, 1995.

[24] I. Masubuchi, A. Ohara, and N. Suda. Lmi-based controller synthesis: A unified formulation and solution. *International Journal of Robust and Nonlinear Control*, 8:669–686, 1998.

[25] Qingqing Miao, Qihui Bian, Bo Qi, and Tao Tang. Direct error observation compensator for visual servo tracking system with image sensor-based sparse measurement. *IEEE Sensors Journal*, 25(7):11441–11450, 2025.

[26] K. Ogata. *Discrete-Time Control Systems*. Prentice-Hall, 2 edition, 1995.

[27] Kouhei Ohnishi. Robust motion control by disturbance observer. *Journal of Robotics and Mechatronics*, 8:218–225, 06 1996.

[28] Chee Khiang Pang, Weili Yan, and Chunling Du. Multirate identification of mechanical resonances beyond the nyquist frequency in high-performance mechatronic systems. *IEEE Transactions on Systems, Man, and Cybernetics: Systems*, 46(4):573–581, 2016.

[29] Sigurd Skogestad and Ian Postlethwaite. *Multivariable Feedback Control: Analysis and Design*. Wiley-Interscience., 2 edition, 2005.

[30] Liting Sun, Tianyu Jiang, and Xu Chen. Adaptive loop shaping for wideband disturbances attenuation in precision information storage systems. *IEEE Transactions on Magnetics*, 53(5):1–13, 05 2017.

[31] T. Tang, S. Xu Niu, T. Yang, B. Qi, and Q. Liang Bao. Vibration rejection of tip-tilt mirror using improved repetitive control. *Mechanical Systems and Signal Processing*, 116:432–442, 2019.

[32] Yi Tang, Wenli Yao, Poh Chiang Loh, and Frede Blaabjerg. Design of lcl filters with lcl resonance frequencies beyond the nyquist frequency for grid-connected converters. *IEEE Journal of Emerging and Selected Topics in Power Electronics*, 4(1):3–14, 2016.

[33] C. Vogel, D. Draxelmayr, and G. Kubin. Spectral shaping of timing mismatches in time-interleaved analog-to-digital converters. In *2005 IEEE International Symposium on Circuits and Systems*, pages 1394–1397 Vol. 2, 2005.

[34] Masashi Wakaiki, Kunihisa Okano, and João P. Hespanha. Stabilization of systems with asynchronous sensors and controllers. *Automatica*, 81:314–321, 2017.

[35] Neng Wan, Dapeng Li, and Naira Hovakimyan. A simplified approach to analyze complementary sensitivity tradeoffs in continuous-time and discrete-time systems. *IEEE Transactions on Automatic Control*, 65(4):1697–1703, 2020.

[36] Zhaoqing Wang, Tianqing Wan, Sijie Ma, and Yang Chai. Multidimensional vision sensors for information processing. *Nature Nanotechnology*, 19(7):919–930, 2024.

[37] P.A. Weaver and R.M. Ehrlich. The use of multi-rate notch filters in embedded-servo disk drives. In *Proceedings of 1995 American Control Conference - ACC'95*, volume 6, pages 4156–4160 vol.6, 1995.

[38] Li Wen, Tianrong Xu, Yong Ruan, Tao Tang, and Hu Yang. Disturbance feedforward control of tip-tilt mirror with gyro measuring for large-amplitude vibration rejection. *IEEE Sensors Journal*, 22(16):16351–16358, 2022.

[39] Matthew T. White, Masayoshi Tomizuka, and C. Smith. Improved track following in magnetic disk drives using a disturbance observer. *IEEE-ASME Transactions on Mechatronics*, 5:3–11, 2000.

[40] Shao-Po Wu, S. Boyd, and L. Vandenberghe. Fir filter design via semidefinite programming and spectral factorization. In *Proceedings of 35th IEEE Conference on Decision and Control*, volume 1, pages 271–276 vol.1, 1996.

[41] Feng Xia and Wenhong Zhao. Flexible time-triggered sampling in smart sensor-based wireless control systems. *Sensors*, 7(11):2548–2564, 2007.

[42] Hui Xiao, Tianyu Jiang, and Xu Chen. Rejecting fast narrow-band disturbances with slow sensor feedback for quality beam steering in selective laser sintering. *Mechatronics*, 56:166–174, 2018.

[43] Kaoru Yamamoto, Li Wen, and Tao Tang. Disturbance rejection beyond the nyquist frequency under sensing delay: Application to an image-based stabilization system. In *IECON 2025 – 51st Annual Conference of the IEEE Industrial Electronics Society*, pages 1–6, 2025.

[44] Kaoru Yamamoto, Yutaka Yamamoto, and Masaaki Nagahara. Hypertracking and hyperrejection: Control of signals beyond the nyquist frequency. *IEEE Transactions on Automatic Control*, 68(10):6232–6239, 2023.

[45] Chia-Pang Yen, Yingming Tsai, and Xiaodong Wang. Wideband spectrum sensing based on sub-nyquist sampling. *IEEE Transactions on Signal Processing*, 61(12):3028–3040, 2013.

[46] Yuan Yuan, Xu Chen, and J. Tang. Multivariable robust blade pitch control design to reject periodic loads on wind turbines. *Renewable Energy*, 146:329–341, 2020.

[47] Yijiu Zhao, Yu Hen Hu, and Jingjing Liu. Random triggering-based sub-nyquist sampling system for sparse multiband signal. *IEEE Transactions on Instrumentation and Measurement*, 66(7):1789–1797, 2017.